PHYSICS OF FLUIDS **27**, 034107 (2015)

Vortex dynamics in a pipe T-junction: Recirculation and sensitivity

Kevin K. Chen,[a] Clarence W. Rowley,[b] and Howard A. Stone[c]
Department of Mechanical and Aerospace Engineering, Princeton University, Princeton, New Jersey 08544, USA

(Received 18 February 2015; accepted 12 March 2015; published online 30 March 2015)

In the last few years, many researchers have noted that regions of recirculating flow often exhibit particularly high sensitivity to spatially localized feedback. We explore the flow through a T-shaped pipe bifurcation—a simple and ubiquitous, but generally poorly understood flow configuration—and provide a complex example of the relation between recirculation and sensitivity. When $Re \geq 320$, a phenomenon resembling vortex breakdown occurs in four locations in the junction, with internal stagnation points appearing on vortex axes and causing flow reversal. The structure of the recirculation is similar to the traditional bubble-type breakdown. These recirculation regions are highly sensitive to spatially localized feedback in the linearized Navier–Stokes operator. The flow separation at the corners of the "T," however, does not exhibit this kind of sensitivity. We focus our analysis on the Reynolds number of 560, near the first Hopf bifurcation of the flow. © *2015 AIP Publishing LLC*. [http://dx.doi.org/10.1063/1.4916343]

I. INTRODUCTION

In the last several years, sensitivity analyses of stability eigenvalues have been a significant focus in the study of flow instability. In particular, Giannetti and Luchini[1] introduced the *sensitivity to spatially localized feedback*, often called the "structural sensitivity," the region of which is called the "wavemaker" or "instability core." The sensitivity to spatially localized feedback has far-reaching implications not only in stability theory but also in feedback flow control and the physical understanding of flow phenomena.

A number of researchers have studied the wavemaker in a variety of recirculating flows and have observed a connection between recirculation and feedback sensitivity. The first observations[1,2] were made for cylinder wakes, revealing that closed particle trajectories exhibited particularly high feedback sensitivity. One experimental study[3] of a swirling jet undergoing vortex breakdown used a local stability analysis to locate the wavemaker upstream of the recirculation bubble. Another study of the same flow configuration,[4] however, perhaps more appropriately used a global analysis, showing that the wavemaker exists in a region that begins upstream of the recirculation and continues somewhat into the bubble. Recent studies have also analyzed the flow through a "mixing" T-shaped pipe junction with two inlets and one outlet,[5] as well as the flow through an X-shaped channel junction with three inlets and one outlet.[6] In these examples, the flow configurations contain comparatively straightforward recirculation regions: the closed orbits are simple loops, or otherwise, the flow is largely unidirectional and can be represented with two spatial dimensions, and the recirculation region is small. These studies observed that recirculating regions are highly sensitive to spatially localized feedback, particularly near the boundaries of such regions.

[a]Electronic mail: kkchen@alumni.princeton.edu. Present address: Department of Aerospace and Mechanical Engineering, University of Southern California, Los Angeles, California 90089, USA.
[b]Electronic mail: cwrowley@princeton.edu
[c]Electronic mail: hastone@princeton.edu

In the case of such simple recirculation streamlines, Ref. 2 proposed to explain the coincidence between recirculation and sensitivity using an inviscid short-wavelength approximation.[7] According to this theory, closed orbits lead to the positive feedback of short-wavelength instabilities, thus creating large changes in the flow. In this manuscript, we take an opposing approach and discuss a complex flow in which we observe the relation between recirculation and sensitivity. The flow we consider is fully three-dimensional and contains features including multiple counter-rotating vortex pairs, large three-dimensional recirculation regions with very high swirl and strong counterflow, vortex breakdown, and multiple interior stagnation points. The coincidence between recirculation and sensitivity suggests that the application of feedback flow control in recirculation regions could be particularly effective, even in flows with complex streamlines.

The flow geometry and conditions that we study are ordinary and appear uncomplicated. T-shaped pipe bifurcations—such as the one shown in Figure 1(a)—are a common flow configuration in both natural and man-made systems. Familiar examples of such flow bifurcations in the natural world include the pulmonary and basilar arteries in the human body. The basilar artery is particularly intriguing, since aneurysms may occur at junctions when the artery walls are weak;[9] see Ref. 10 for a study on flows through pipe bifurcations resembling blood vessel branches. Among man-made systems, examples include microfluidic channels for heat transfer, industrial pipe networks, and other fluid distribution systems in buildings. Despite the universality of the T-junction flow and the closely related L-bend, a large gap in the physical understanding of these flows persists. Many previous studies[10–14] offer detailed images and basic physical insight, particularly as they relate to laminar flows with modest Reynolds numbers. Yet, few provide quantitative characterizations tied to the physical behavior in these flows.

A recent insight into T-shaped pipe bifurcation flows, however, is the discovery of recirculation arising from internal stagnation points,[15] which we take as the signature of the "bubble-type" of vortex breakdown. In this study, a predominantly liquid flow enters the main branch of the "T" and exits from the two symmetric side branches. The flow traps suspended gas bubbles in vortical structures near stagnation regions when the Reynolds number, based on the average inlet speed, is above approximately 350. The trapping occurs because of flow recirculation with the characteristics of vortex breakdown, as well as large pressure gradients and drag forces on the bubbles in the junction.

This bubble trapping phenomenon merits a further investigation of the single-phase T-junction flow. In this manuscript, we investigate how the recirculation in such a flow is connected to the sensitivity to spatially localized feedback. We emphasize that although there exists geometric similarity among the "impacting" T-shaped pipe junction with one inlet and two outlets, the "mixing" T-shaped pipe junction with two inlets and one outlet,[5] and the mixing X-shaped channel junction with three inlets and one outlet,[6] the latter two cases do not exhibit vortex breakdown. Our global

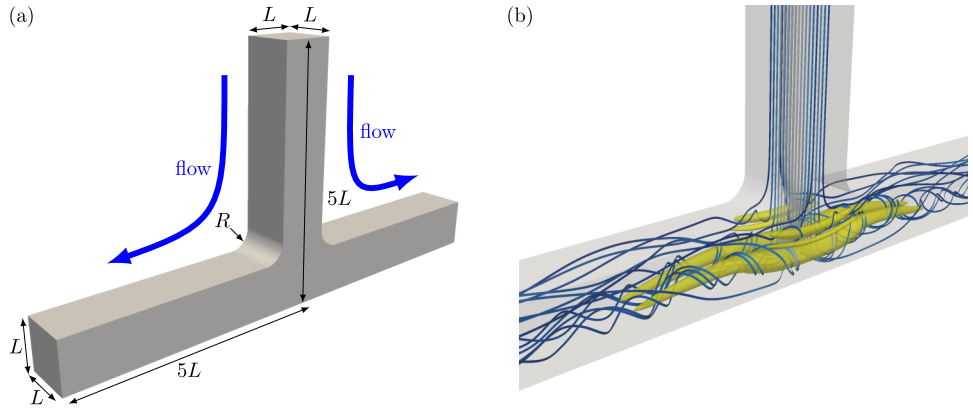

FIG. 1. (a) The T-junction geometry. (b) Velocity streamlines (white: high speed; blue: medium speed; black: low speed) at $Re = 560$, with $R = 0.4L$. Given the Frobenius norm $\|\cdot\|_F$, we also define $Q = (\|\nabla\mathbf{u} - (\nabla\mathbf{u})^T\|_F^2 - \|\nabla\mathbf{u} + (\nabla\mathbf{u})^T\|_F^2)/8$ and depict a single level set of Q (yellow); see Ref. 8 for a discussion of vortex identification.

analysis shows that although the impacting T-junction flow's recirculation regions are not simple streamline loops, they do still essentially coincide with the sensitivity regions, which is the main contribution of this paper. We focus on Reynolds numbers where the steady-state solution loses stability, but the flow remains laminar. We also briefly comment on the effects of the junction corners' radius of curvature.

This manuscript is organized as follows. In Sec. II, we review the theory of sensitivity to spatially localized feedback. We briefly comment on the computational setup and algorithms in Sec. III, and we describe the vortex breakdown, recirculation, and sensitivity of the T-junction flow in Sec. IV. Finally, we conclude with a brief summary in Sec. V.

II. SENSITIVITY TO SPATIALLY LOCALIZED FEEDBACK

To define the sensitivity, we employ a linear framework. Given the average inlet flow speed U, the pipe width L (see Figure 1(a)), and the kinematic viscosity ν, we define the Reynolds number $Re = UL/\nu$. The Navier–Stokes operator $\mathcal{N}$ is given by the equation

$$\dot{\mathbf{u}} = \mathcal{N}\mathbf{u} = -\mathbf{u}\cdot\nabla\mathbf{u} - \nabla p + Re^{-1}\nabla^2\mathbf{u} \tag{1}$$

and is subject to the continuity equation $\nabla\cdot\mathbf{u} = 0$ and a set of boundary conditions, which we describe for the T-junction flow in Sec. III. We assume that there exists some steady-state velocity field $\mathbf{u}_0$, such that $\mathcal{N}\mathbf{u}_0 = \mathbf{0}$. We then linearize the operator $\mathcal{N}$ about $\mathbf{u}_0$ to derive the linearized Navier–Stokes operator $\mathcal{L}$ for the velocity and pressure perturbations $\mathbf{u}'$ and p', given by

$$\dot{\mathbf{u}}' = \mathcal{L}\mathbf{u}' = -\mathbf{u}'\cdot\nabla\mathbf{u}_0 - \mathbf{u}_0\cdot\nabla\mathbf{u}' - \nabla p' + Re^{-1}\nabla^2\mathbf{u}'; \tag{2}$$

this is subject to $\nabla\cdot\mathbf{u}' = 0$ and typically homogeneous boundary conditions. If we are further given some control volume Ω and the complex conjugate operator $\overline{(\cdot)}$, then we can define the inner product

$$\langle\mathbf{u}_1,\mathbf{u}_2\rangle = \int_\Omega \mathbf{u}_1\cdot\bar{\mathbf{u}}_2\,\mathrm{d}V, \tag{3}$$

from which we define the adjoint $\mathcal{L}^*$ of the operator $\mathcal{L}$. Denoting the adjoint velocity and pressure perturbations by $\hat{\mathbf{u}}'$ and $\hat{p}'$, the adjoint equation is

$$\dot{\hat{\mathbf{u}}}' = \mathcal{L}^*\hat{\mathbf{u}}' = -(\nabla\mathbf{u}_0)\cdot\hat{\mathbf{u}}' + \mathbf{u}_0\cdot\nabla\hat{\mathbf{u}}' - \nabla\hat{p}' + Re^{-1}\nabla^2\hat{\mathbf{u}}', \tag{4}$$

subject to $\nabla\cdot\hat{\mathbf{u}}' = 0$ and a suitable set of boundary conditions with which the adjoint relation $\langle\mathcal{L}\mathbf{u}',\hat{\mathbf{u}}'\rangle = \langle\mathbf{u}',\mathcal{L}^*\hat{\mathbf{u}}'\rangle$ is satisfied.[1,16]

We define the sensitivity of the linearized dynamics to spatially localized feedback using a global mode analysis.[1] If the direct and adjoint eigendecompositions are $\mathcal{L}\boldsymbol{\phi}_j = \lambda_j\boldsymbol{\phi}_j$ and $\mathcal{L}^*\boldsymbol{\psi}_j = \bar{\lambda}_j\boldsymbol{\psi}_j$, respectively, then an infinitesimal perturbation of the former yields

$$\delta\mathcal{L}\,\boldsymbol{\phi}_j + \mathcal{L}\,\delta\boldsymbol{\phi}_j = \delta\lambda_j\,\boldsymbol{\phi}_j + \lambda_j\,\delta\boldsymbol{\phi}_j. \tag{5}$$

Following the definition in (3), the inner product of (5) with $\boldsymbol{\psi}_j$ leads to a cancellation of the second terms on the left- and right-hand sides, i.e.,

$$\left\langle\delta\mathcal{L}\,\boldsymbol{\phi}_j,\boldsymbol{\psi}_j\right\rangle = \left\langle\delta\lambda_j\,\boldsymbol{\phi}_j,\boldsymbol{\psi}_j\right\rangle. \tag{6}$$

Let us further restrict $\delta\mathcal{L}$ to be a spatially localized feedback mechanism. Given the Dirac delta function δ_D, some perturbation location $\boldsymbol{\xi}$, and some perturbation size δs, we set $\delta\mathcal{L} = \delta_\mathrm{D}(\mathbf{x}-\boldsymbol{\xi})\,\delta s$. This perturbation could be, for instance, the application of feedback control with a collocated actuator and sensor. From (6), it follows that

$$\boldsymbol{\phi}_j(\boldsymbol{\xi})\cdot\bar{\boldsymbol{\psi}}_j(\boldsymbol{\xi})\,\delta s = \delta\lambda_j\left\langle\boldsymbol{\phi}_j,\boldsymbol{\psi}_j\right\rangle. \tag{7}$$

Therefore, we may define a *sensitivity function*

$$\zeta_j(\mathbf{x}) = \frac{d\lambda_j}{ds} = \frac{\boldsymbol{\phi}_j(\mathbf{x})\cdot\bar{\boldsymbol{\psi}}_j(\mathbf{x})}{\left\langle\boldsymbol{\phi}_j,\boldsymbol{\psi}_j\right\rangle}, \tag{8}$$

which dictates the change in the jth eigenvalue as a result of spatially localized feedback at the location $\mathbf{x}$, with strength δs. The physical locations where $|\zeta_j(\mathbf{x})|$ is large are the regions where the dynamics are especially sensitive to these feedback mechanisms.

III. COMPUTATIONAL SETUP

To approximate the steady-state solution $\mathbf{u}_0$ for a given Re, we employ a Newton–Armijo iteration[17,18] on the operator $\mathcal{N}$ (1) over the vector space of spatially discretized velocity fields $\mathbf{u}$. We compute the Newton solver's initial condition either by running a time-resolved flow solver for a long time or from a zeroth- or first-order extrapolation of solutions at other Reynolds numbers. Within the Newton solver itself, we use the Generalized Minimal Residual (GMRES) method[18,19] to solve the Jacobian–vector equation $d\mathcal{N}/d\mathbf{u}|_{\mathbf{u}_k} \cdot \mathbf{h} = -\mathcal{N}\mathbf{u}_k$ for the Newton step $\mathbf{h}$ from the kth Newton iterate $\mathbf{u}_k$. To compute the Jacobian–vector product $d\mathcal{N}/d\mathbf{u}|_{\mathbf{u}_k} \cdot \mathbf{h}$, we use a "time-stepping" approach,[20] employing the finite difference $d\mathcal{N}/d\mathbf{u}|_{\mathbf{u}_k} \cdot \mathbf{h} = (\mathcal{N}(\mathbf{u}_k + \epsilon\mathbf{h}) - \mathcal{N}\mathbf{u}_k)/\epsilon + O(\epsilon)$, with $\epsilon = 10^{-3}$. We terminate the Newton–Armijo search when $\mathbf{u}_k$ satisfies $\|\mathcal{N}\mathbf{u}_k\|_2/V < 10^{-6}$, where $\|\mathbf{u}\|_2 = \sqrt{\langle \mathbf{u}, \mathbf{u} \rangle}$ (see (3)) and V is the volume of the domain Ω.

Once we have obtained a satisfactory approximation for $\mathbf{u}_0$, we employ an Arnoldi iteration[21] with discrete-time variants of $\mathcal{L}$ (2) and $\mathcal{L}^*$ (4) to approximate their leading eigenvalues and eigenmodes. In our computation, 100 Arnoldi iterations are sufficient for good convergence of the leading 25 or so modes; with 800 iterations, virtually no change in the leading eigenvalues is apparent. Numerically, $\mathcal{L}^*$ is a continuous adjoint operator. For the five least stable eigenvalues of $\mathcal{L}$, the mismatch between the corresponding eigenvalues of $\mathcal{L}$ and $\mathcal{L}^*$ is between 0.05% and 2% of the direct eigenvalue's magnitude, with a mean of 0.8%; these errors are consistent with the numerically resolved simulations of Ref. 22. Also, we remark that when we compute any of the Navier–Stokes operators on a velocity field, we first solve for the pressure field using the divergence of the corresponding Eqs. (1), (2), and (4).

We implement the Navier–Stokes operators (1), (2), and (4) using software based on the OpenFOAM suite's icoFoam solver.[23] This solver uses the finite-volume Pressure-Implicit with Splitting of Operators (PISO) method,[24–26] which predicts the updated velocity at each time step based on the current pressure field and corrects the velocity and pressure to satisfy continuity. Typically, the average volume integral of $|\nabla \cdot \mathbf{u}|$ in a finite volume cell is on the order of 10^{-8}. The mesh is unstructured, with quantities defined at cell centers. The solver, however, also interpolates fluxes on cell boundaries to evaluate spatial differentiation and nonlinear advection and employs cell surface integration to compute divergence operators. We employ second-order accurate temporal and spatial derivatives, and the time advancement is fully implicit. Although the PISO algorithm is more primitive than other available algorithms, it provides sufficient accuracy for the linear stability analysis we seek.

The T-junction geometry we study has a square cross-section to match experiments,[15] but our results may extend to other cross-sections as well. The cross-section has dimensions $L \times L$, and the inlet and two outlets are each $5L$ long; see Figure 1(a). A shortening of the inlet to $3L$ and an extension of the outlets to $10L$ individually show little difference in the flow behavior and the eigenvalues of $\mathcal{L}$ and $\mathcal{L}^*$. In our investigation, we focus on a junction corner radius of curvature $R = 0.4L$ (see Figure 1(a)) to match our experimental work, but we also examine the flow with $R = 0$ (i.e., a square corner) and $R = L$. The geometries have 5 459 520 finite-volume cells with $R = 0$, 6 096 840 cells with $R = 0.4L$ and 7 435 776 cells with $R = L$. The mesh is finer near the junction and the walls, where gradients are large, and coarser near the inlet and outlets, where gradients in the inflow and outflow directions are small. Finer meshes do produce very small changes in velocity and pressure profiles, as well as in the eigenvalues of $\mathcal{L}$ and $\mathcal{L}^*$. Setting $Re = 560$ and $R = 0.4L$, we compare the leading eigenvalue of $\mathcal{L}$ using the "medium" 6 096 840-cell mesh, as well as a coarser 3 143 056-cell mesh and a finer 12 082 728-cell mesh. Denoting the respective leading eigenvalues with the coarse, medium, and fine mesh by λ_c, λ_m, and λ_f, we find that $|\lambda_m - \lambda_f| = 2.42 \cdot 10^{-2}$ and $|\lambda_c - \lambda_f| = 6.34 \cdot 10^{-2}$. We stress that the qualitative nature of our solutions, which is the topic of this manuscript, is unaffected by further grid refinement.

In the nonlinear Navier–Stokes operator $\mathcal{N}$, we impose at the inlet the square Poiseuille velocity profile $\mathbf{u}$ and pressure gradient $\mathbf{n} \cdot \nabla p$,[27] with $\mathbf{n}$ the outward normal vector of the simulation domain. We further impose $\mathbf{u} = \mathbf{0}$ and $\mathbf{n} \cdot \nabla p = 0$ at the walls and $\mathbf{n} \cdot \nabla \mathbf{u} = \mathbf{0}$ and $p = 0$ at the outlets. The linearized operator $\mathcal{L}$ has the same conditions on $\mathbf{u}'$ and p', except that $\mathbf{u}' = \mathbf{0}$ and $\mathbf{n} \cdot \nabla p' = 0$ at the inlet. Finally, the adjoint $\mathcal{L}^*$ has the same boundary conditions as $\mathcal{L}$ on $\hat{\mathbf{u}}'$ and $\hat{p}'$, except that $(\mathbf{u}_0 \cdot \mathbf{n})\hat{\mathbf{u}}' + Re^{-1}\mathbf{n} \cdot \nabla \hat{\mathbf{u}}' = \mathbf{0}$ at the outlets to satisfy the adjoint relation $\langle \mathcal{L}\mathbf{u}', \hat{\mathbf{u}}' \rangle = \langle \mathbf{u}', \mathcal{L}^*\hat{\mathbf{u}}' \rangle$.

IV. RESULTS

A. Base flow

At $Re = O(10^2)$, the flow retains the square Poiseuille profile in the inlet pipe. It features a significant secondary flow, however, consisting of a large counter-rotating vortex pair in the junction, which extends toward the outlets. Figure 1(b) depicts these flow features with streamlines and vortex visualization. Additional counter-rotating vortex pairs are also present, such as the secondary and tertiary pair visible in Figure 1(b).

The computed steady-state solutions remain stable until the first Hopf bifurcation occurs at $Re = 587$ for the junction corner radius of curvature $R = 0$, $Re = 556$ for $R = 0.4L$, and $Re = 552$ for $R = L$; see Figure 2. This figure also depicts further Hopf bifurcations of the steady-state solution after the first instability; note that these bifurcations will not be observed experimentally, since the steady-state solutions there are unstable. In this laminar flow regime, an increase in Re generally increases the sensitivity of the linearized dynamics to spatially localized feedback.[1] The increase in Reynolds number triggers an increase in non-normality, potentially causing ϵ-scale perturbations in $\mathcal{L}$ to shift eigenvalues of $\mathcal{L}$ by considerably more than ϵ.[28] We will see that the regions of large sensitivity are intrinsically connected to recirculation regions in the flow.

At $Re \geq 320$, four of these recirculation regions appear in the junction, with one in each outlet–depth quadrant. This behavior was first reported in single-phase numerical simulations inspired by a bubble-laden T-junction flow[15] and is shown in Figure 3 near the first Hopf bifurcation. The recirculation arises as a result of a phenomenon resembling a bubble-type vortex breakdown behavior, where internal stagnation points appear on the axes of vortices. We note that the vortex breakdown in the T-junction has some resemblance to the classical bubble-type breakdown,[29] but the structure has distinct differences. The classical bubble-type breakdown contains an approach flow in the same direction as the bubble's vortex core. On the other hand, each vortex breakdown bubble in the T-junction is flush with the center plane between the two outlets, prohibiting the existence of a traditional approach flow. Instead, the approach toward each breakdown bubble is from the inlet flow, which is perpendicular to the vortex cores; see Figure 3(a).

In the outlet pipes, stagnation points mark the sudden transition from tightly swirling regions with flow reversal to downstream vortices that primarily flow toward the outlets. Four of these

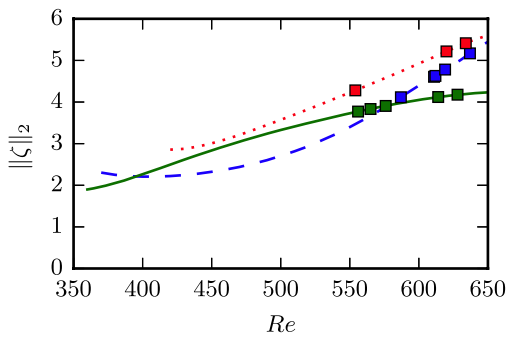

FIG. 2. The sensitivity function's L_2 norm $\|\zeta\|_2 = (\int_\Omega |\zeta|^2 \mathrm{d}V)^{1/2}$ (see (8)), as the center (i.e., neutrally stable) mode at the first Hopf bifurcation numerically continues to Re below and above the Hopf bifurcation. Blue dashed line: $R = 0$; green solid line: $R = 0.4L$; and red dotted line: $R = L$. Hopf bifurcations are shown as squares.

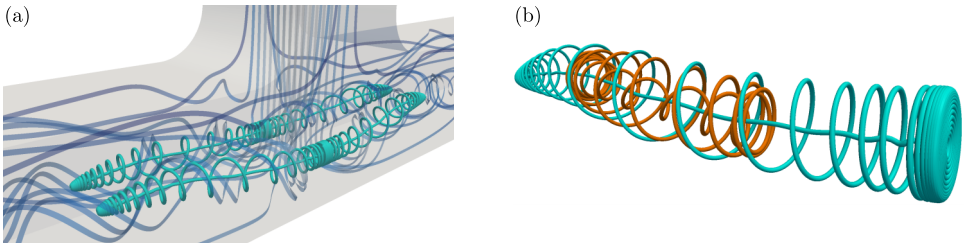

FIG. 3. The vortex breakdown at $Re = 560$ and $R = 0.4L$ using a refined mesh with 13 291 412 cells. (a) Streamlines of the four recirculation regions (cyan), with additional streamlines as in Figure 1(b). (b) An outer (cyan) and inner (orange) streamline from a single recirculation region. The cyan streamline's left end is an outlet stagnation point; the right side is flush with the T-junction's center plane and also contains a stagnation point at the center.

stagnation points, which we call "outlet stagnation points," are found at the points in the outlet pipes where the vortex breakdown bubble terminates and the flow turns backwards; see the left extent of the recirculation regions in Figure 3. Each outlet stagnation point is a saddle-type fixed point with a two-dimensional stable manifold comprising the boundary of the recirculation region and a one-dimensional unstable manifold carrying fluid either toward the outlet or back toward the center plane between the two outlets.

This center plane, as visible on the right side of Figure 3(b), is an invariant set, since the flow is symmetric about it. On this plane, additional stagnation points also appear in the vortex cores. The recirculation dynamics on this plane consist of unstable fixed points enclosed by periodic orbits. The unstable manifolds of these periodic orbits delimit the boundaries of the recirculation regions. These unstable manifolds appear to be coincident with the stable manifolds of the outlet stagnation points, as the long, horizontal shell of the recirculation region in Figure 3(b) demonstrates.

If these manifolds are coincident, then there is no transport of fluid particles into or out of the recirculation regions, whereas if these manifolds intersect transversely, then the resulting lobe dynamics provide a mechanism for entrainment and detrainment.[30,31] Reference 31 found that it is necessary to do a very careful mesh refinement to determine if the manifolds are in fact coincident. For the corner radius $R = 0.4L$, we perform a mesh refinement in a region that extends approximately $0.15L$ beyond the recirculation regions. By doubling the grid resolution in each of the three spatial dimensions within this region, we increase the resolution of the recirculation regions from 1 027 796 cells to 8 222 368 cells, such that the refined region has a resolution of approximately $404 \times 98 \times 196$. (The resolution in the three dimensions is not precisely defined, because the mesh is not a simple Cartesian one.) With the refinement, the entire grid contains 13 291 412 finite volume cells. The refined region is even finer than the $153 \times 97 \times 97$ grid that Ref. 31 employed not just for their vortex breakdown structure but rather for their entire domain. Despite this refinement, we detected neither lobe dynamics nor transport in or out of the recirculation region. Hence, we believe that the stable manifolds of the outlet stagnation points do in fact coincide with the unstable manifolds of the center plane's periodic orbits.

B. Sensitivity to spatially localized feedback

The qualitative nature of the T-junction flow's recirculation streamlines has significant implications for the sensitivity of the flow dynamics, since there is a dense family of closed streamline orbits. At present, researchers have observed a connection between recirculation and high sensitivity to spatially localized feedback in simple closed orbits, such as in stationary[1] and periodic[2] flows behind a cylinder. The use of the inviscid short-wavelength theory[7] to explain such a connection would be restricted to such simple orbits. In contrast, a rigorous application of the theory to the T-junction flow would be extremely difficult. Not only do the orbits shown in Figure 3 exhibit tight swirl and significant counterflow but also a single streamline inside the recirculation region would likely densely fill a two-dimensional manifold. Furthermore, the low local Reynolds numbers in the vortices would render the inviscid approximation invalid.

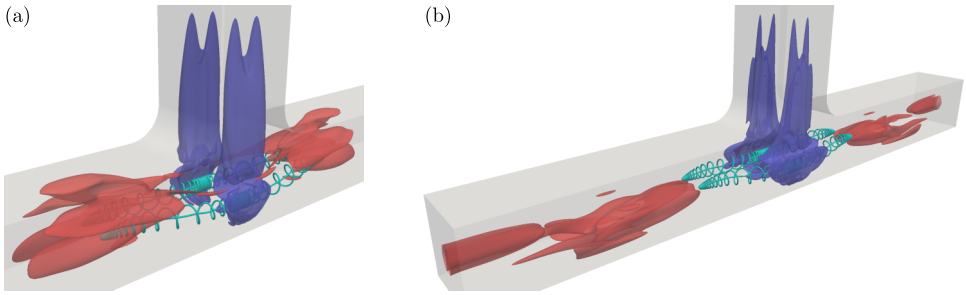

FIG. 4. A level set of the direct eigenmode magnitude $\|\boldsymbol{\phi}\|$ (red) and the adjoint eigenmode magnitude $\|\boldsymbol{\psi}\|$ (blue), with recirculation streamlines (cyan), at $Re = 560$ and $R = 0.4L$. (a) The least stable mode. (b) The second least stable mode.

Nevertheless, the recirculation and sensitivity regions of the T-junction flow do coincide very closely, despite the complexity of the underlying flow. Figure 4 shows the direct and adjoint eigenmodes used in the computation of the sensitivity, and Figure 5 shows the relation between the recirculation and the sensitivity. This figure shows the sensitivity regions of the two least stable modes with $R = 0.4L$ and $Re = 560$, near the first Hopf bifurcation. Figure 5(b) specifically shows that the highest sensitivity of the flow actually exists in lobes in the exterior, not the interior, of the vortices. Such a feature is in agreement with previous studies in recirculation and sensitivity for simpler flows.[1,4,6] A comparison of Figures 1(b) and 5(a) reveals that the sensitivity to spatially localized feedback is also large in the secondary and tertiary counter-rotating vortex pairs that appear above the large primary pair. Although these vortex pairs neither undergo vortex breakdown nor constitute recirculation regions, the swirl in these pairs is very large compared to the axial velocity. We posit that this swirl may contribute to the locally increased sensitivity in a similar way to the recirculation regions.

Examining the sensitivity regions of the next several modes, we find very little qualitative change. The sensitivity of the second instability (Figure 5(c)), as well as the third and fourth instabilities (not shown), is more pronounced away from the center plane between the two outlets. We remark that Ref. 5 had reported a coincidence between recirculation and sensitivity when the flow direction in the T-junction is reversed, though vortex breakdown does not appear in the reversed flow.

At this point, it is clear that the recirculation regions are key aspects of the T-junction flow. Nevertheless, what is the role of the flow separation at the junction corners? Figure 6(a) shows the vortical

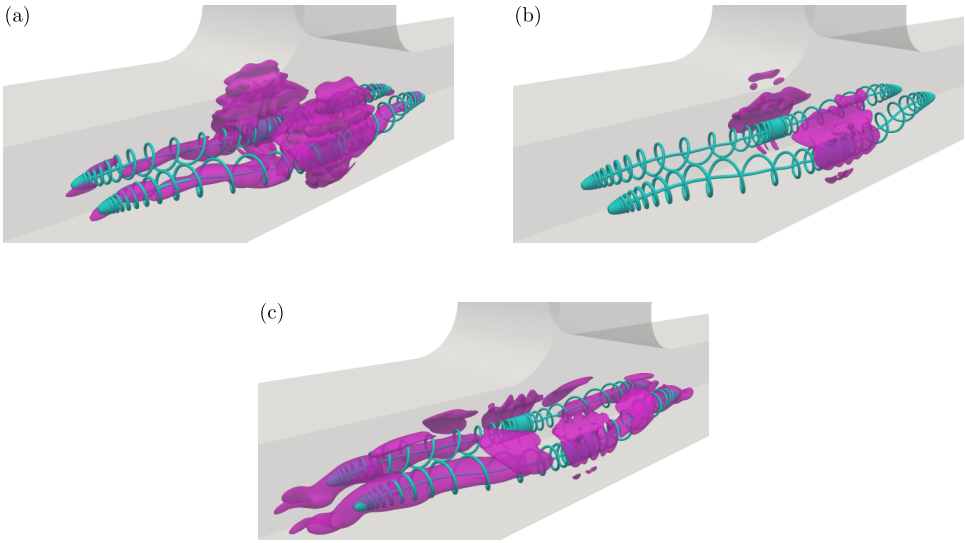

FIG. 5. Level sets of the sensitivity magnitude $|\zeta|$ (magenta), with recirculation streamlines (cyan), at $Re = 560$ and $R = 0.4L$. (a) The least stable mode, showing $|\zeta| = 2$ and (b) $|\zeta| = 6$. (c) The second least stable mode, showing $|\zeta| = 2.75$.

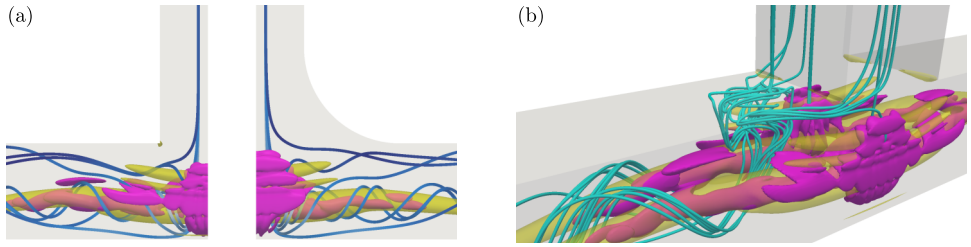

FIG. 6. (a) As Figures 1(b) and 5, but with $R = 0$ and $Re = 590$ (left) and $R = L$ and $Re = 550$ (right). Only half of each domain is shown for brevity. (b) The flow with $R = 0$ and $Re = 590$, with additional streamlines (cyan) depicting the flow separation at the left square corner.

flow and the sensitivity of the first instability at the first Hopf bifurcation, for the square corner $R = 0$ and the large radius of curvature $R = L$. In these cases, the qualitative nature of the sensitivity regions is nearly identical to that of the intermediate radius of curvature $R = 0.4L$ (Figure 5).

Additional insight may be possible if we visualize the velocity streamlines comprising the separation regions at the square corners for $R = 0$. In Figure 6(b), a particular set of streamlines starts near the walls of the inlet, navigates around the square corner of the junction, and encounters an adverse pressure gradient in the outlet pipes. This pressure gradient causes these streamlines to turn backward, forming a vertical vortex pair that flushes fluid downward between the two large recirculation regions in the junction. The critical observation in this case is that the separation region—which does not contain recirculation—lies completely outside the region of high sensitivity. Similar flow features also occur for $R = 0.4L$ and $R = L$ (not shown), where the separation region is much smaller.

Since the separation and sensitivity regions are distinct, the flow separation at the corners is "inert" in the sensitivity analysis. Infinitesimal dynamical perturbations in the separation region will not have significant effects on the steady-state flow's stability, even though the separation is a prominent feature of the flow. In comparison, the recirculation regions in the junction enable small dynamical perturbations there to have large effects on global stability. We posit that the flow near the junction corners does not possess sufficient swirl to support large sensitivity.

V. CONCLUSION

We computed a global linear sensitivity analysis of a complex flow through a pipe T-junction. When $Re \geq 320$, the junction contains four instances of a bubble-type vortex-breakdown-like flow feature, where the dynamics are highly sensitive to spatially localized feedback, especially near the boundaries of the recirculation regions. An important implication of this connection is that even in flows with multiple counter-rotating vortex pairs, vortex breakdown, internal stagnation points, high swirl, complicated streamline patterns, and strong counterflow, the application of flow control in recirculation regions may be especially effective. In the T-junction flow, the four vortex breakdown bubbles resemble that of classical bubble-type breakdown but lack the typically associated approach flow. Instead, each bubble begins at the center plane between the two outlets and suddenly terminates at an interior stagnation point. Secondary and tertiary vortex pairs also exhibit high sensitivity, possibly because of high swirl. The junction corners' radius of curvature does not have a significant effect on the flow sensitivity, however, and the flow separation at the junction corners lies outside the regions of high sensitivity.

In a separate paper, we will comment on additional details of our analysis, including a full description of the numerical setup, grid refinement, and validation. The upcoming manuscript will also describe the vortex behavior—including vortex profiles, swirl angles, and pressure gradients—in greater detail. Furthermore, we will analyze the eigenvalues and eigenmodes, including the growth rate and frequency sensitivity to spatially localized feedback, and we will discuss the flow's sensitivity to base flow modifications. All of these aspects serve to amplify the main theme of this paper, which is that even in flows with complex streamlines, recirculation regions exhibit high eigenvalue sensitivity and have important implications for flow control. These stability and sensitivity analyses will yield

new insight into the behavior of this very common, though complex and at times counterintuitive flow.

ACKNOWLEDGMENTS

K.K.C. was funded by the National Science Foundation through the Graduate Research Fellowship Program, with additional support from the Viterbi Postdoctoral Fellowship through the University of Southern California's Viterbi School of Engineering. We thank Stefan Radl and Daniele Vigolo for their assistance, and François Gallaire and Paolo Luchini for discussions regarding vortex breakdown, instability types, and sensitivity. We also thank Philip Holmes, John O. Dabiri, Matthew O. Williams, and Jonathan H. Tu for their insight into the recirculation streamlines. Finally, we appreciate the insight and suggestions provided by Paul K. Newton, as well as reviewers of previous versions of this manuscript. We performed the computation on clusters at Princeton University's TIGRESS High Performance Computing Center, and we created flow visualizations using ParaView.

[1] F. Giannetti and P. Luchini, "Structural sensitivity of the first instability of the cylinder wake," J. Fluid Mech. **581**, 167–197 (2007).
[2] F. Giannetti, S. Camarri, and P. Luchini, "Structural sensitivity of the secondary instability in the wake of a circular cylinder," J. Fluid Mech. **651**, 319–337 (2010).
[3] K. Oberleithner, M. Sieber, C. N. Nayeri, C. O. Paschereit, C. Petz, H.-C. Hege, B. R. Noack, and I. Wygnanski, "Three-dimensional coherent structures in a swirling jet undergoing vortex breakdown: Stability analysis and empirical mode construction," J. Fluid Mech. **679**, 383–414 (2011).
[4] U. A. Qadri, D. Mistry, and M. P. Juniper, "Structural sensitivity of spiral vortex breakdown," J. Fluid Mech. **720**, 558–581 (2013).
[5] A. Fani, S. Camarri, and M. V. Salvetti, "Investigation of the steady engulfment regime in a three-dimensional T-mixer," Phys. Fluids **25**, 064102 (2013).
[6] I. Lashgari, O. Tammisola, V. Citro, M. P. Juniper, and L. Brandt, "The planar X-junction flow: Stability analysis and control," J. Fluid Mech. **753**, 1–28 (2014).
[7] A. Lifschitz and E. Hameiri, "Local stability conditions in fluid dynamics," Phys. Fluids A **3**, 2644–2651 (1991).
[8] P. Chakraborty, S. Balachandar, and R. J. Adrian, "On the relationships between local vortex identification schemes," J. Fluid Mech. **535**, 189–214 (2005).
[9] A. H. Ropper and M. A. Samuels, *Adams and Victor's Principles of Neurology*, 9th ed. (McGraw-Hill, 2009), Chap. 34.
[10] T. Karino, H. L. Goldsmith, M. Motomiya, S. Mabuchi, and Y. Sohara, "Flow patterns in vessels of simple and complex geometries," Ann. N. Y. Acad. Sci. **516**, 422–441 (1987).
[11] S. M. Senn and D. Poulikakos, "Laminar mixing, heat transfer and pressure drop in tree-like microchannel nets and their application for thermal management in polymer electrolyte fuel cells," J. Power Sources **130**, 178–191 (2004).
[12] N. Kockmann, M. Engler, D. Haller, and P. Woias, "Fluid dynamics and transfer processes in bended microchannels," Heat Transfer Eng. **26**, 71–78 (2005).
[13] D. Haller, P. Woias, and N. Kockmann, "Simulation and experimental investigation of pressure loss and heat transfer in microchannel networks containing bends and T-junctions," Int. J. Heat Mass Transfer **52**, 2678–2689 (2009).
[14] D. Doorly and S. Sherwin, "Geometry and flow," *Cardiovascular Mathematics*, Modeling, Simulation and Applications edited by L. Formaggia, A. Quarteroni, and A. Veneziani (Springer, 2009), Vol. 1, Chap. 5.
[15] D. Vigolo, S. Radl, and H. A. Stone, "Unexpected trapping of particles at a T junction," Proc. Natl. Acad. Sci. U. S. A. **111**, 4770–4775 (2014).
[16] D. C. Hill, "A theoretical approach for analyzing the restabilization of wakes," *NASA Technical Memorandum* 103858, National Aeronautics and Space Administration, Ames Research Center, Moffett Field, CA, 1992.
[17] L. Armijo, "Minimization of functions having Lipschitz continuous first partial derivatives," Pac. J. Math. **16**, 1–3 (1966).
[18] C. T. Kelley, *Iterative Methods for Linear and Nonlinear Equations*, Frontiers in Applied Mathematics (Society for Industrial and Applied Mathematics, Philadelphia, PA, 1995), Vol. 16.
[19] Y. Saad and M. H. Schultz, "GMRES: A generalized minimal residual algorithm for solving nonsymmetric linear systems," SIAM J. Sci. Stat. Comput. **7**, 856–869 (1986).
[20] L. Tuckerman and D. Barkley, "Bifurcation analysis for timesteppers," in *Numerical Methods for Bifurcation Problems and Large-Scale Dynamical Systems*, The IMA Volumes in Mathematics and its Applications Vol. 119 (Springer-Verlag, 2000), pp. 453–466.
[21] L. N. Trefethen and D. Bau III, *Numerical Linear Algebra* (Society for Industrial and Applied Mathematics, Philadelphia, PA, 1997).
[22] G. J. Chandler, M. P. Juniper, J. W. Nichols, and P. J. Schmid, "Adjoint algorithms for the Navier–Stokes equations in the low Mach number limit," J. Comput. Phys. **231**, 1900–1916 (2012).
[23] H. H. Weller, G. Tabor, H. Jasak, and C. Fureby, "A tensorial approach to computational continuum mechanics using object-oriented techniques," Comput. Phys. **12**, 620–631 (1998).
[24] R. I. Issa, "Solution of the implicitly discretised fluid flow equations by operator-splitting," J. Comput. Phys. **62**, 40–65 (1986).
[25] R. I. Issa, A. D. Gosman, and A. P. Watkins, "The computation of compressible and incompressible recirculating flows by a non-iterative implicit scheme," J. Comput. Phys. **62**, 66–82 (1986).

[26] J. H. Ferziger and M. Perić, *Computational Methods for Fluid Dynamics*, 3rd ed. (Springer-Verlag, Berlin, Heidelberg, New York, NY, 2002).
[27] F. M. White, *Viscous Fluid Flow*, 3rd ed. (McGraw-Hill, Inc., New York, NY, 2005).
[28] J.-M. Chomaz, "Global instabilities in spatially developing flows: Non-normality and nonlinearity," Annu. Rev. Fluid Mech. **37**, 357–392 (2005).
[29] S. Leibovich, "The structure of vortex breakdown," Annu. Rev. Fluid Mech. **10**, 221–246 (1978).
[30] P. Holmes, "Some remarks on chaotic particle paths in time-periodic, three dimensional swirling flows," Contemp. Math. **28**, 393–404 (1984).
[31] F. Sotiropoulos, Y. Ventikos, and T. C. Lackey, "Chaotic advection in three-dimensional stationary vortex-breakdown bubbles: Šil'nikov's chaos and the devil's staircase," J. Fluid Mech. **444**, 257–297 (2001).